Processing and Application of Ceramics 18 [2] (2024) 224–233
https://doi.org/10.2298/PAC2402224J

Effects of different processing parameters on structure of $Ba_{1-x}Sr_xTiO_3$ powders synthesized via nonhydrolytic sol-gel method

Feng Jiang[1,*], Entao Zheng[1], Guo Feng[1,*], Qing Yang[1], Wenwei Jin[1], Chuan Shao[2], Jianmin Liu[1], Dahai Wang[3], Jian Liang[1]

[1]*Department of Material Science and Engineering, Jingdezhen Ceramic University, Jingdezhen 333000, China*
[2]*Jingdezhen Comprehensive Inspection and Testing Center, Jingdezhen 333000, China*
[3]*Jingdezhen Oceano Ceramic Company, Jingdezhen 333000, China*

Received 21 January 2024; Received in revised form 14 June 2024; Accepted 23 June 2024

Abstract

The rapid development of miniaturization and refinement of modern electronic components has led to higher requirements for nanosized powders. The barium strontium titanate ($Ba_{1-x}Sr_xTiO_3$, BST) nanopowders with fine grains, uniform particle size and high purity have broad application prospects. Herein, BST nanopowders were synthesized via nonhydrolytic sol-gel method and the effects of different processing parameters on structure were investigated systematically by using X-ray diffraction, transmission electron microscopy, laser particle size analyser and thermogravimetric mass spectrometry. In the first step, different dispersants, dispersant concentration and calcination temperature were selected for synthesis of $Ba_{0.6}Sr_{0.4}TiO_3$ powder to find optimal conditions. In the second step, these optimal conditions were used to synthesize BST powders, but different (Ba+Sr)/Ti and Ba/Sr molar ratios were used to find those that can enable preparation of single phase cubic perovskite powder. Therefore, this study showed how the processing parameters can be systematically tuned with the idea to obtain ultra-fine single phase BST nanoparticles.

Keywords: *nonhydrolytic sol-gel method, $Ba_{1-x}Sr_xTiO_3$ powders, synthesis optimization*

I. Introduction

Barium strontium titanate (BST) ceramics is a piezoelectric ceramics with excellent performance [1,2]. It has both the characteristics of high dielectric constant and low dielectric loss of $BaTiO_3$ and the stable characteristics of $SrTiO_3$. It is widely used in microwave phase shifters, capacitors, resonators and wide fields [3–6]. The performance requirements for BST ceramic materials are also increasing, with the continuous development of science and technology. The performance and reliability of BST ceramics-based devices are closely related to the morphology, phase purity, composition and crystallinity of BST powders [7].

The route and conditions for $Ba_{1-x}Sr_xTiO_3$ powders synthesis have great influence on their performance [8,9]. High-quality BST powders generally have the characteristics of high phase purity homogeneous particle size. The preparation of high-quality BST ceramic ultra-fine powders is the premise and foundation for high-performance BST ceramics [10,11]. The traditional solid phase method [12] is generally used to prepare BST powders. This method is not suitable for preparing BST high-performance ceramics because of its large particle size, high content of aggregates and impurities. However, the current trend of miniaturization of electronic components requires that the particle size is usually less than 100 nm [13]. Synthesis methods for preparation of BST powders with narrow particle size distribution, good dispersion and high phase purity have been researched, including the hydrothermal method [14], citrate method [15], sol-gel method [16] and nonhydrolytic sol-gel method (NHSG method) [17]. However, the hydrothermal method is more prone to side reactions, and the equipment requirements are high. The citric acid method has low temperature and

* Corresponding author: tel: +86 798 8499328
e-mail: *jiangfeng@jci.edu.cn* (F. Jiang),
fengguo@jci.edu.cn (G. Feng)

small particle size, but it is greatly affected by pH value and dispersant. The hydrolytic sol-gel method can achieve homogeneous mixing at molecular level, but the hydrolysis rate of each component is not easy to control. The NHSG method can be used for synthesis of $Ba_{1-x}Sr_xTiO_3$ powders at low temperature via atomic-level uniform mixing, which makes it a promising method for preparing high quality BST powders.

In our previous work [18] we have started to investigate the effects of raw material types and some of parameters in nonhydrolytic sol-gel synthesis on the structure of $Ba_{0.6}Sr_{0.4}TiO_3$ powders. Based on that, in this work those investigations are systematized and expanded to $Ba_{1-x}Sr_xTiO_3$ powders. Accordingly, a novel type of ultra-fine BST nanopowders were developed by the nonhydrolytic sol-gel method assisted by the addition of dispersant, which improved the low temperature synthesis effect and the composition uniformity.

II. Experimental

2.1. Material and methods

Raw materials, used in experimental part, were all purchased from Sinopharm Chemical Reagent Co. Ltd. and are of AR grade. In the first part of this work, different dispersants, dispersant concentration and calcination temperature were selected for synthesis of $Ba_{0.6}Sr_{0.4}TiO_3$ powder to find optimal conditions for preparation of very fine powder. Barium acetate ($Ba(CH_3COO)_2$) and strontium acetate ($Sr(CH_3COO)_2$) were weighed into a conical flask and dissolved in glycerol ($C_3H_8O_3$). Butyl titanate ($Ti(OC_4H_9)_4$) was poured into another conical flask with 50 ml glycerol. Both of them were placed on the magnetic stirrer and stirred for 10 min. Then, the barium acetate and strontium acetate solution were poured into the butyl titanate solution and stirred evenly to obtain a mixed solution. The following cation ratio in solution was used: Ba/Sr/Ti = 0.6/0.4/1.2. Subsequently, surfactant was added in amount of 1.0 wt.% in relation to the total mass of the precursors and stirred for 15 min. Different surfactants were analysed: PEG 1000 (CP, Shanghai), Tween 60 (CP, Shanghai) and Span 80 (CP, Shanghai). In addition, different concentrations of the selected surfactant were used (0.5, 1.0, 1.5 and 2.0 wt.%) to determine the optimal one. The flask of the mixed solution was then placed in a constant temperature digital display oil bath at 110 °C for 24 h to obtain an orange precursor sol. Furthermore, the precursor sol was distilled at 250 °C for 6 h with the formation of a black xerogel. Finally, the xerogel was ground and calcined at different temperatures: 700, 800, 900 and 1000 °C for 2 h.

In the second part of this work, the selected optimal conditions were used to synthesize BST powers with different Ba/Sr molar ratios (i.e. $Ba_{1-x}Sr_xTiO_3$, where x = 0.2, 0.3, 0.4, 0.5) and the influence of (Ba+Sr)/Ti molar ratios were analysed to find optimal one for preparation of a single phase perovskite powder.

2.2. Characterization

X-ray diffraction (XRD, DX-2700B, Dandong Haoyuan Instrument Co. Ltd, China) with Cu-K_α radiation (wavelength of 0.154 nm) was used to analyse the crystal phase composition of the samples. The measuring 2θ range was 10–70° and scanning time 10 min with a stepping angle of 0.02°. For the Rietveld refinement, the stepping scan rate was increased to 6 s and other parameters remained unchanged.

A laser particle size analyser (Mastersizer 3000, Malvern Company, UK) was employed to characterized particle sizes and distribution. The particle size distribution width was measured by *Span* parameter, which was calculated according to the following equation [19]:

$$Span = \frac{D_{90} - D_{10}}{D_{50}} \quad (1)$$

where, D_{10}, D_{50} and D_{90} are particles sizes at 10%, 50% and 90% in cumulative distribution, respectively. The closer the *Span* value is to 0, the more uniform the particle size is, and the higher the particle size uniformity. On the contrary, larger *Span* values indicate worse uniformity.

Surface area was characterized by low-temperature nitrogen adsorption (ASAP2020M, Micromeritics, USA) by Brunaure-Emmett-Teller method. High resolution transmission electron microscopy (HR-TEM, JEM-2010, JEOL, Japan) was used to obtain high-resolution transmission electron microscopy images. DTA-TG instrumen (STA 449C, NETZSCH, Germany) equipped with a mass spectrometer (QMS403C, NETZSCH, Germany) was employed to characterize the thermogravimetric effects of xerogel in the heating process. The heating rate was 10 °C/min and the final temperature was 1000 °C.

III. Results and discussion

3.1. Effect of dispersant type

This research group has successfully prepared single phase $Ba_{0.6}Sr_{0.4}TiO_3$ powders before [18], so in this work we used the $Ba_{0.6}Sr_{0.4}TiO_3$ powders for the further study the influence of dispersant type on particle sizes and distribution. Figure 1 shows XRD patterns of the samples prepared with different dispersants: Span 80, Tween 60 and PEG 1000, with the concentration of 1.0 wt.% to the total mass of the precursors. The calcination temperature of the samples was 900 °C. XRD pattern of the sample prepared without dispersant is also presented in Fig. 1 for comparison. It can be seen that the addition of dispersant has little effect on the phase composition of samples, and no other phase except for $Ba_{0.6}Sr_{0.4}TiO_3$ phase (JCPDS 34-0411) in all samples was detected. However, compared with the sample without dispersant, the diffraction peaks of the samples with a dispersant have higher intensity and narrower width, which indicates that the samples have higher crystallinity.

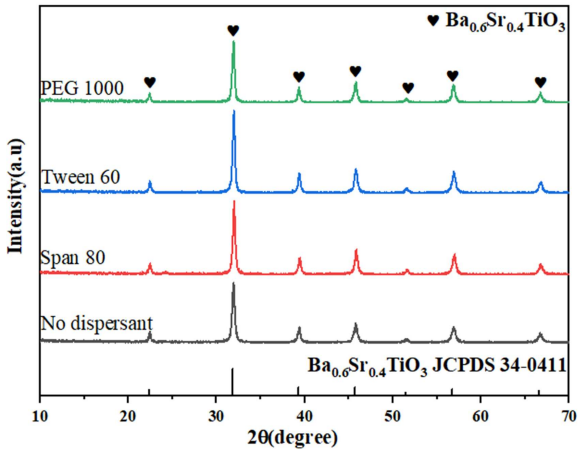

Figure 1. XRD patterns of samples prepared with different dispersants (amount of dispersants: 1 wt.%, calcination temperature: 900 °C)

Figure 2 shows the particle size distribution of the $Ba_{0.6}Sr_{0.4}TiO_3$ powders prepared with different dispersants. It can be seen that the portion of particles smaller than 2 μm in the sample without dispersant is 94.1%, whereas the portions of those particles are 98.5%, 99.4% and 98.1% for the powders synthesized with Span 80, Tween 60 and PEG 1000, respectively. In addition, all particle sizes of the samples with Span 80, Tween 60 and PEG 1000 are less than 10 μm, which is not the case for the sample without dispersant. These results indicate that the addition of dispersant makes the size distribution of the $Ba_{0.6}Sr_{0.4}TiO_3$ powders more uniform and improve dispersibility of particles in glycerol. When the nanoparticles are close to each other, the existing adsorption layer will be compressed to generate repulsive force, thus preventing the agglomeration between the nanoparticles [20].

Furthermore, as it can be also seen from Fig. 2 the D_{10}, D_{50} and D_{90} of the samples prepared with Tween 60 as a dispersant are smaller than those with other dispersants. The reason can be different molecular structure of the selected dispersants (Fig. 3). Thus, in comparison with PEG 1000, Tween 60 and Span 80 have terminal "anchor" structures of polyhydroxy and polyalkoxy groups. They also have multiple "anchor" active sites, which is convenient for molecular "anchors" to be fixed on the surface of colloidal particles. At the same time, compared to Span 80, Tween 60 has no double bond at the tail alkyl position, which enables better flexibility of the tail molecule than that of

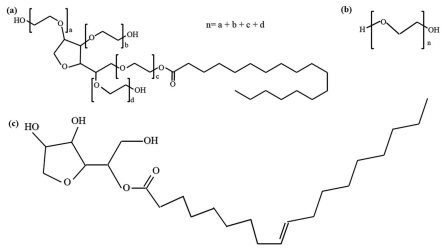

Figure 3. Molecular structural formula of Tween 60 (a), PEG 1000 (b) and Span 80 (c)

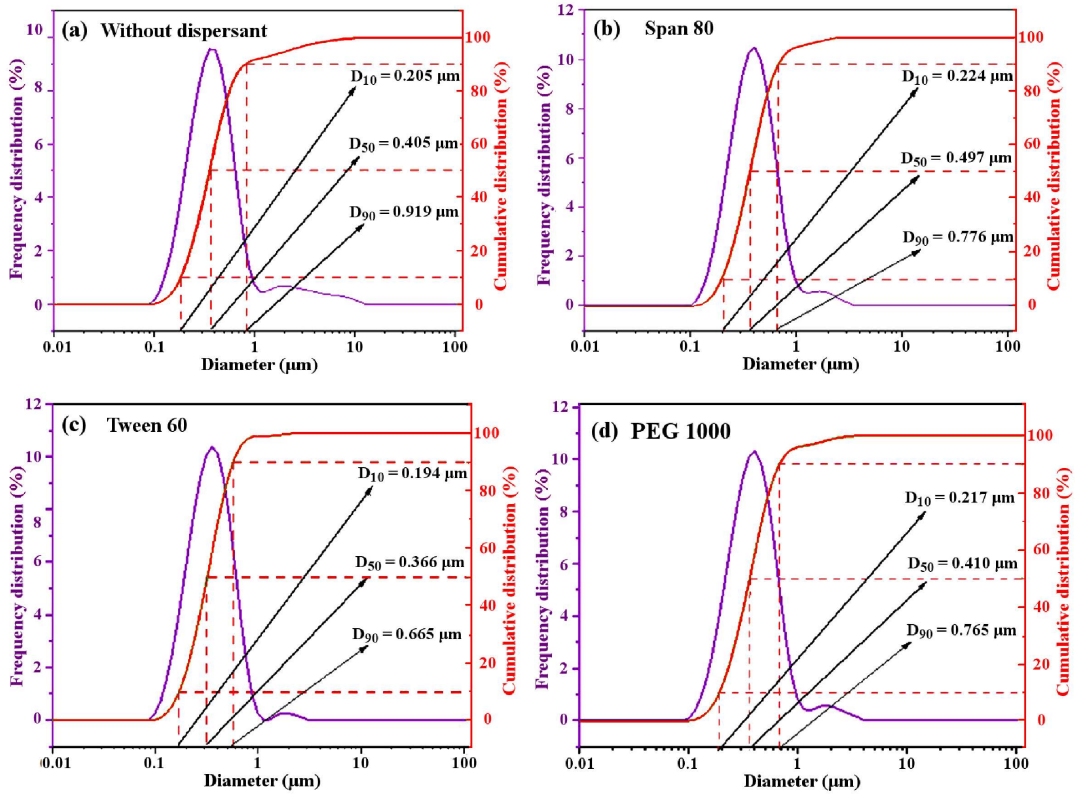

Figure 2. Particle size distribution of samples prepared with different dispersants: a) without dispersant, b) Span 80, c) Tween 60 and d) PEG 1000 (amount of dispersants: 1 wt.%, calcination temperature: 900 °C)

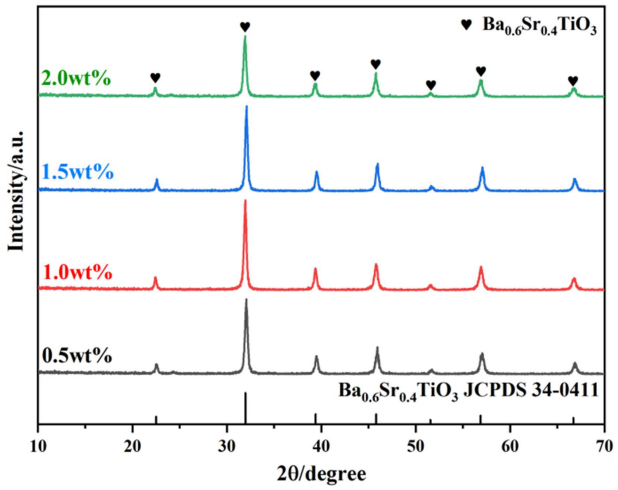

Figure 4. XRD patterns of samples prepared with different amounts of Tween 60 (calcination temperature: 900 °C)

Span 80. The better flexibility is more conducive to the full opening of the molecular chain, playing full steric hindrance of long-chain molecules and avoiding cross-entanglement of molecules to cause aggregation. These results and analysis confirm that Tween 60 is better than other two dispersants.

3.2. *Effect of Tween 60 concentration*

XRD patterns of the samples prepared with different concentration (0.5, 1.0, 1.5 and 2.0 wt.%) of Tween 60 and calcined at 900 °C are presented in Fig. 4. It clearly shows that there is no obvious influence of the Tween 60 addition amount on crystallinity of the $Ba_{0.6}Sr_{0.4}TiO_3$ phase. However, as it can be seen from Fig. 5, the amount of Tween 60 has influence on the particle size distribution of the samples. This is because Tween 60, as a surface modifier, can be adsorbed on the surface of $Ba_{0.6}Sr_{0.4}TiO_3$ particles as a growth inhibitor to prevent the agglomeration and hinder the excessive growth [21]. The calculated *Span* values for the samples with 0.5, 1.0, 1.5 and 2.0 wt.% Tween 60 are 1.774, 1.287, 1.320 and 1.385, respectively, and the smallest particle sizes have the samples with 1.0 and 1.5 wt.% Tween 60. These results can be explained by the electrostatic repulsion force of the electric double layer on the surface of nanoparticles which is the largest at these dispersant amounts. However, when the dispersant addition amount is higher, supersaturated adsorption will be generated at the nanoparticle surface. In this case, the attraction between particles will be greater than the repulsive force between electric double layers, and the particles will agglomerate and settle resulting in poor uniformity [21]. Therefore, we selected 1.0 wt.% as an optimal amount of Tween 60.

3.3. *TEM test and finishing*

Figure 6 shows TEM micrograph of the calcined $Ba_{0.6}Sr_{0.4}TiO_3$ sample prepared without dispersant as well as TEM micrograph, HR-TEM micrograph and SEAD pattern of the same sample with 1.0 wt.% Tween 60 as a dispersant. It can be seen from Figs. 6a and

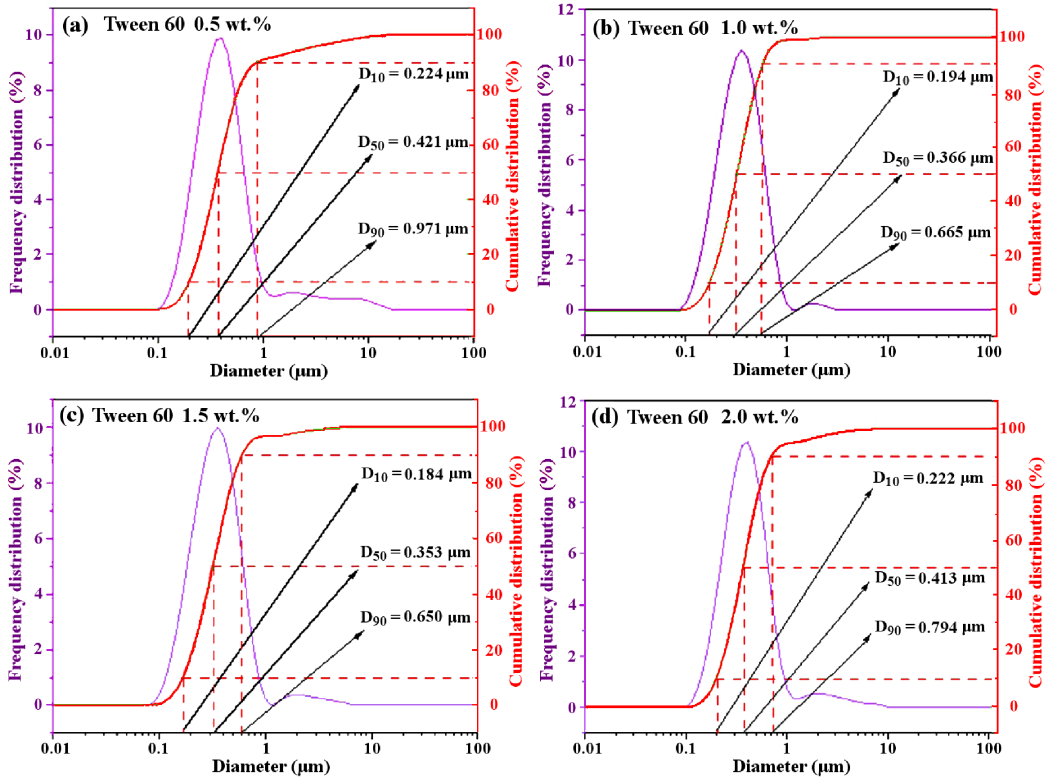

Figure 5. Particle size distribution of samples prepared with different amounts of Tween 60: a) 0.5, b) 1.0, c) 1.5 and d) 2.0 wt.% (calcination temperature: 900 °C)

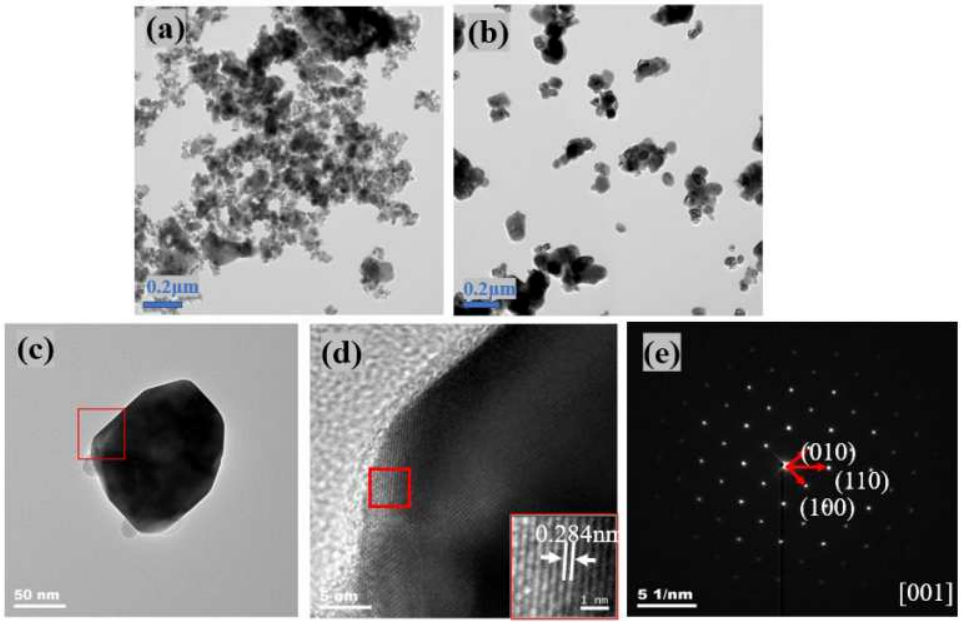

Figure 6. TEM micrographs of samples without dispersant (a) and with 1.0 wt.% Tween 60 (b,c); HR-TEM micrograph (d) and SAED pattern (e) of sample with 1.0 wt.% Tween 60

6b that the dispersion of the $Ba_{0.6}Sr_{0.4}TiO_3$ particles is improved after adding 1.0 wt.% Tween 60. The lattice stripes can be seen in HR-TEM graph shown in Fig. 6d, which indicate the high crystallinity of the $Ba_{0.6}Sr_{0.4}TiO_3$ particles [22]. In addition, the measured crystal plane space is d = 0.284 nm, which is in good agreement with the (110) crystal plane spacing of 0.281 nm from the PDF card of $Ba_{0.6}Sr_{0.4}TiO_3$ (JCPDS 34-0411). Figure 6e clearly shows single crystal structure electron diffraction patterns of the $Ba_{0.6}Sr_{0.4}TiO_3$

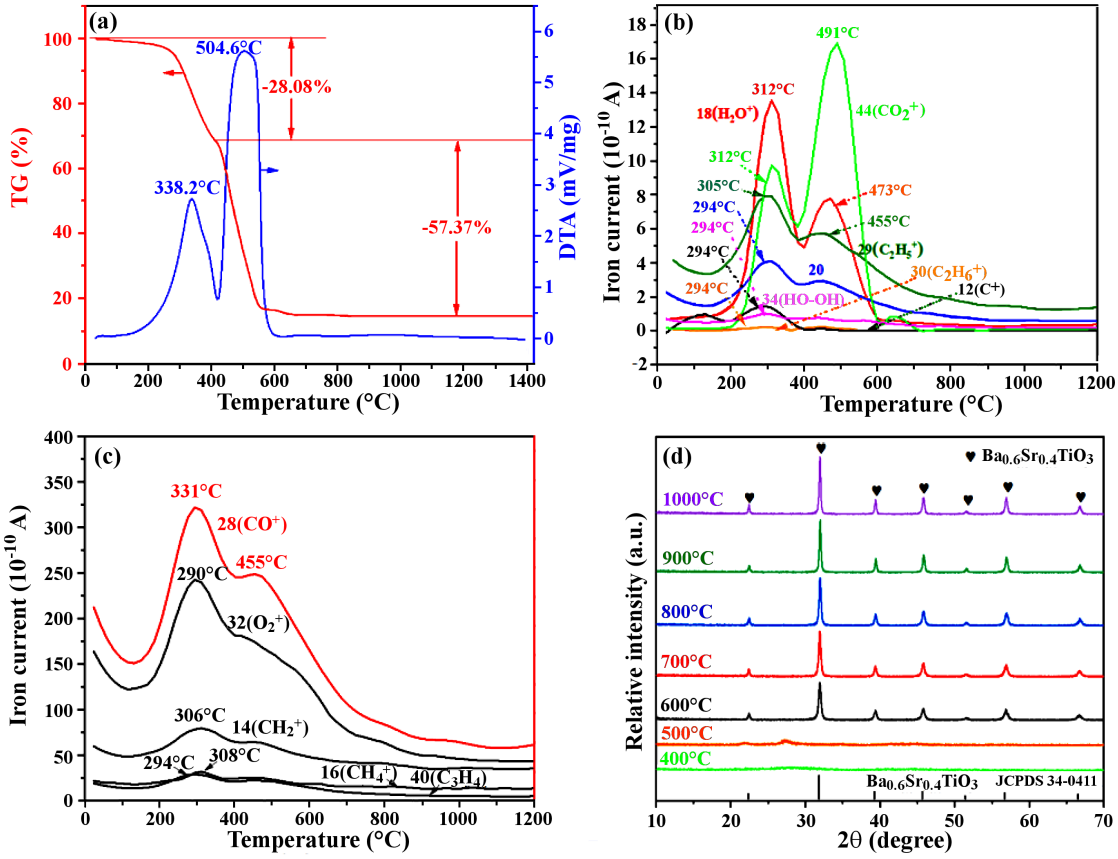

Figure 7. DTA-TG curve of xerogel (a), MS curves of each product during thermal decomposition (b-c) and XRD patterns of samples calcined at different temperatures (d)

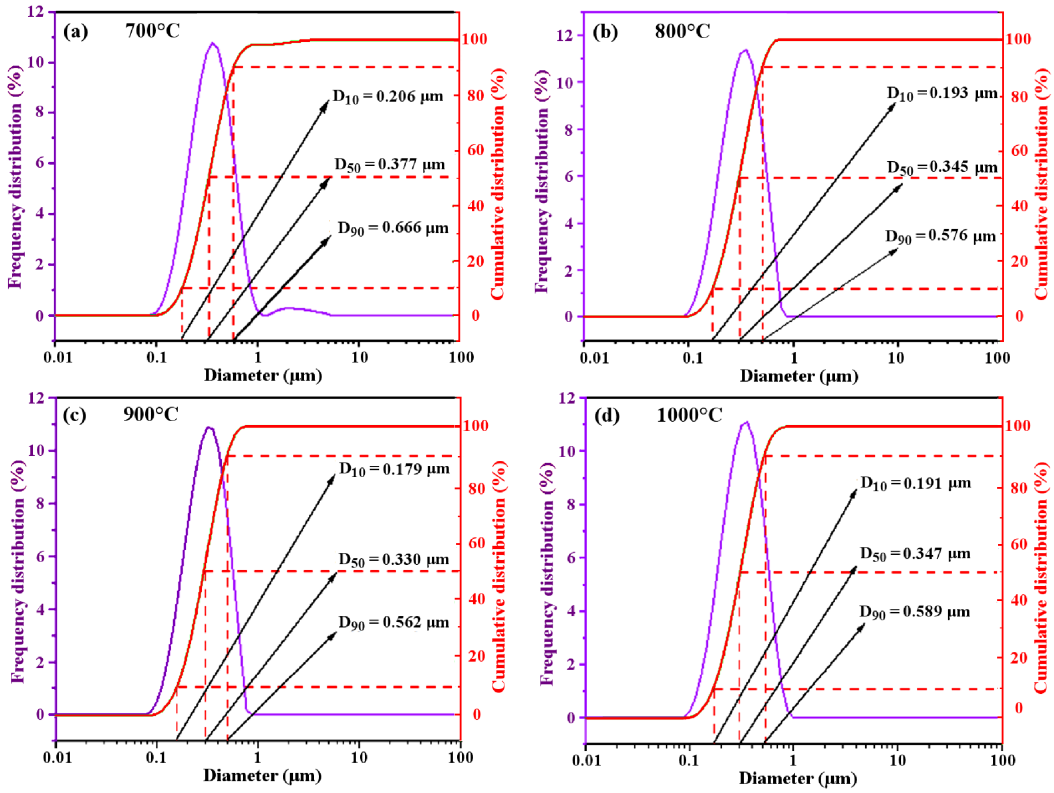

Figure 8. Particle size distribution of barium strontium titanate synthesized at different temperatures: a) 700 °C, b) 800 °C, c) 900 °C and d) 1000 °C (type of dispersant: Tween 60, amount of dispersant: 1 wt.%)

with 1.0 wt.% Tween 60. The smallest array points correspond to (100), (010) and (110) planes of the $Ba_{0.6}Sr_{0.4}TiO_3$ phase, which conform the parallelogram rule of the vector. At the same time, it can be determined that the diffraction direction corresponds to [001] (Fig. 6e). The two-dimensional lattice stripe clearly shows that the nanoparticles are crystalline without dislocation, grain boundary or other defect structures, which further confirms the single crystal property of $Ba_{0.6}Sr_{0.4}TiO_3$ particles [23].

3.4. Effect of calcination temperature

The thermogravimetric effects and the structure of escaping gases during heat the treatment of xerogel were detected by DTA-TG-MS and used to find optimal calcination temperature for preparation of small particles with the highest possible phase purity [24]. Investigation was conducted on the $Ba_{0.6}Sr_{0.4}TiO_3$ powder and the selected type and amount of dispersant were Tween 60 and 1.0 wt.%. The DTA-TG curves in Fig. 7a show that the thermogravimetric effects can be divided into two stages. In the first stage, an exothermic peak at 338.2 °C appears from room temperature to 400 °C, and the corresponding weight loss is 28.08%. It is related to the oxidative combustion of organic groups and substances such as acetate, butoxy and glycerol (boiling point 290 °C). The exothermic peak in the second stage appears at 504.6 °C. Two major exothermic peaks in the first and second stages correspond to the mass spectrometer (MS) curves shown in Figs. 7b and 7c. According to the optimized raw materials [25] used in this work, the following ions and exothermic effects are detected: 14–CH_2^+ (306 °C), 16–CH_4^+ (308 °C), 18–H_2O^+ (312 °C, 473 °C), 28–CO^+ (331 °C, 455 °C), 29–$C_2H_5^+$ (305 °C, 455 °C), 30–$C_2H_6^+$ (294 °C), 32–O_2^+ (290 °C), 34–HO–OH (294 °C), 40–$C_3H_4^+$ (294 °C) and 44–CO_2 (312 °C, 491 °C). It can be seen from the MS curves that a large amount of gas escapes at 200–400 °C and 400–600 °C, corresponding to the DTA-TG curves. Among them, CO (331 °C) has the strongest ionic strength and confirms that the whole system is in a reducing atmosphere and not affected by oxygen in the air. The O in the detected fragment ions (H_2O^+, CO^+, O_2^+, HO–OH, CO_2^+) are all from the residual organic groups [26]. In the second stage, the concentration of CO_2^+ ions increased significantly, possibly because some CO is oxidized to CO_2.

To confirm the reasons for the formation of exothermic peak at 504 °C on the DTA curve, the XRD patterns of the samples calcined at 400–1000 °C with 100 °C interval are shown in Fig. 7d. It can be seen that the samples calcined at 400 and 500 °C are amorphous. Crystalline $Ba_{0.6}Sr_{0.4}TiO_3$ phase (JCPDF 34-0411), without other impurity phases, forms when temperature rises to 600 °C, confirming that the exothermic peak at 504.6 °C is partially caused by the formation of this crystal phase. This temperature is much lower than that in other methods, which is in some cases even 1200 °C [27].

Figure 8 shows the particle size distribution of the samples calcined at 700–1000 °C with 100 °C intervals,

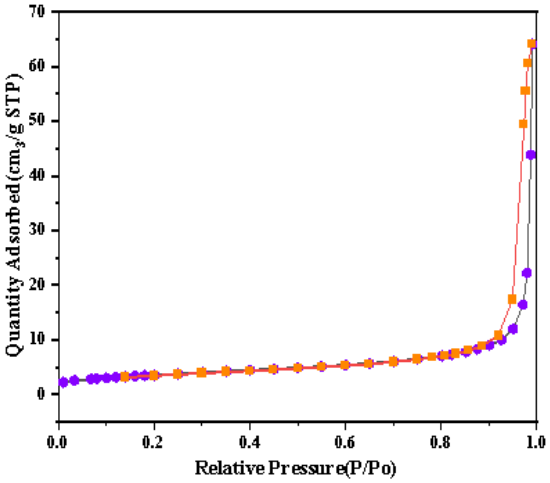

Figure 9. N_2 adsorption-desorption isotherm curves of $Ba_{0.6}Sr_{0.4}TiO_3$ powder

to further confirm the optimal conditions for obtaining powders with uniform and small particle sizes. It can be seen that the powders calcined at lower temperatures have bimodal size distribution, whereas only one main peak exists in the powders calcined at 900 and 1000 °C. The particle sizes of D_{10}, D_{50} and D_{90} of the sample calcined at 900 °C are the smallest. In addition, the escape curves at 900 °C (Figs. 7b and 7c) are relatively flat, indicating that the organic groups are eliminated before 900 °C. Therefore, 900 °C is the optimal calcination temperature.

Figure 9 shows the N_2 adsorption-desorption isotherm curves of the optimized $Ba_{0.6}Sr_{0.4}TiO_3$ sample prepared by the NHSG method. The determined specific surface area is 12.8 m^2/g, which is an ideal value for applications especially in slurry.

3.5. *Effect of Ba/Sr and (Ba+Sr)/Ti ratios*

Figure 10a presents XRD patterns of samples prepared with different Ba/Sr ratios. Among them, the dispersant type, dispersant concentration and calcination temperature were Tween 60, 1 wt.% and 900 °C, respectively. For better comparison, 3D XRD patterns of the samples prepared with different Ba/Sr ratios are shown in Fig. 10b. The main phase of all samples is perovskite $BaTiO_3$ phase (JCPDS 05-0626). In addition, the shift of XRD peaks towards lower 2θ angles with the decrease of Sr content is obvious. According to the Bragg diffraction equation ($2d \cdot \sin\theta = n \cdot \lambda$), the corresponding crystal plane space increases when the diffraction angle decreases, which indicates that strontium enters the barium titanate lattice due to the substitution of larger Ba^{2+} (r = 0.134 nm) with smaller Sr^{2+} (r = 0.112 nm) ions [28]. The pure phase $Ba_{0.6}Sr_{0.4}TiO_3$ was prepared with the optimal (Ba+Sr)/Ti ratio of (0.6+0.4)/1.2. However, there are obvious impurity phases which can be clearly visible in 3D XRD patterns (Fig. 10b). Thus, the samples $Ba_{0.5}Sr_{0.5}TiO_3$ and $Ba_{0.6}Sr_{0.4}TiO_3$ have no impurity phase detected, but diffraction peaks (at 22° < 2θ < 25°) of barium carbonate heterophase are present in the $Ba_{0.8}Sr_{0.2}TiO_3$ and $Ba_{0.7}Sr_{0.3}TiO_3$ samples. In addition, the diffraction peak intensities increase with the increase of Ba ratio.

The (Ba+Sr)/Ti ratio was further adjusted to obtain $Ba_{1-x}Sr_xTiO_3$ pure crystal phase with different Ba/Sr ratios. XRD patterns of the $Ba_{0.7}Sr_{0.3}TiO_3$ and $Ba_{0.8}Sr_{0.2}TiO_3$ samples with different (Ba+Sr)/Ti ratios are shown in Fig. 11. It can be seen that the impurity content of barium carbonate gradually decreases with the increase of the (Ba+Sr)/Ti ratio. Finally, the $Ba_{0.7}Sr_{0.3}TiO_3$ and $Ba_{0.8}Sr_{0.2}TiO_3$ pure phase powders were prepared with (Ba+Sr)/Ti molar ratios of (0.7+0.3)/1.3 and (0.8+0.2)/1.4, respectively.

Figure 12 shows XRD patterns of the $Ba_{1-x}Sr_xTiO_3$ samples with different Ba/Sr ratios and the optimized (Ba+Sr)/Ti molar ratio. It can be seen that there is no barium carbonate impurity diffraction peak at 22°–25°, which indicates that pure phase $Ba_{1-x}Sr_xTiO_3$ powders were formed. The XRD peak intensities increase with the increase of strontium content (Fig. 12c), indicating that the substitution of strontium reduces the crystallinity of BST [29], due to the growth rate of $SrTiO_3$ being faster than that of $BaTiO_3$ [30]. It is important to mention that one single peak is observed and there is no splitting of the XRD peak from (200) plane, indicating that all diffraction peaks belong to the cubic perovskite structure (space group: *Pm3m*). This result is due to the size effect of nanocrystals and stabilization of a high-symmetry phase [31].

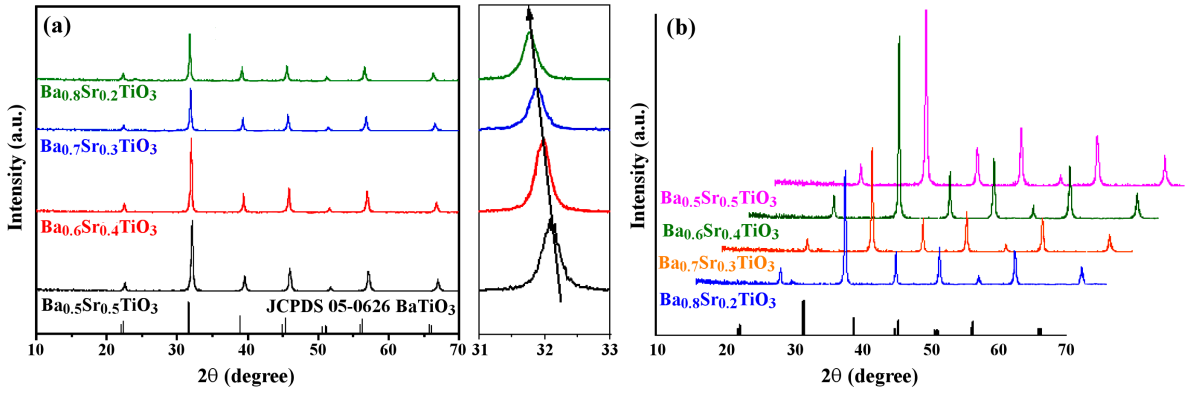

Figure 10. XRD (a) and 3D XRD (b) patterns of samples prepared with different Ba/Sr ratios

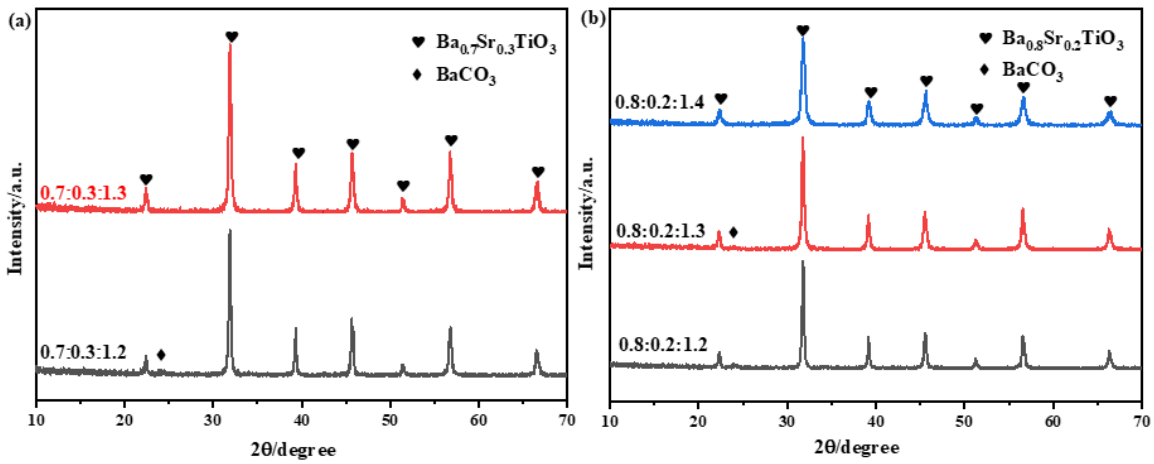

Figure 11. XRD patterns of samples prepared with different Ba/Sr ratios: a) $Ba_{0.7}Sr_{0.3}TiO_3$ and b) $Ba_{0.8}Sr_{0.2}TiO_3$

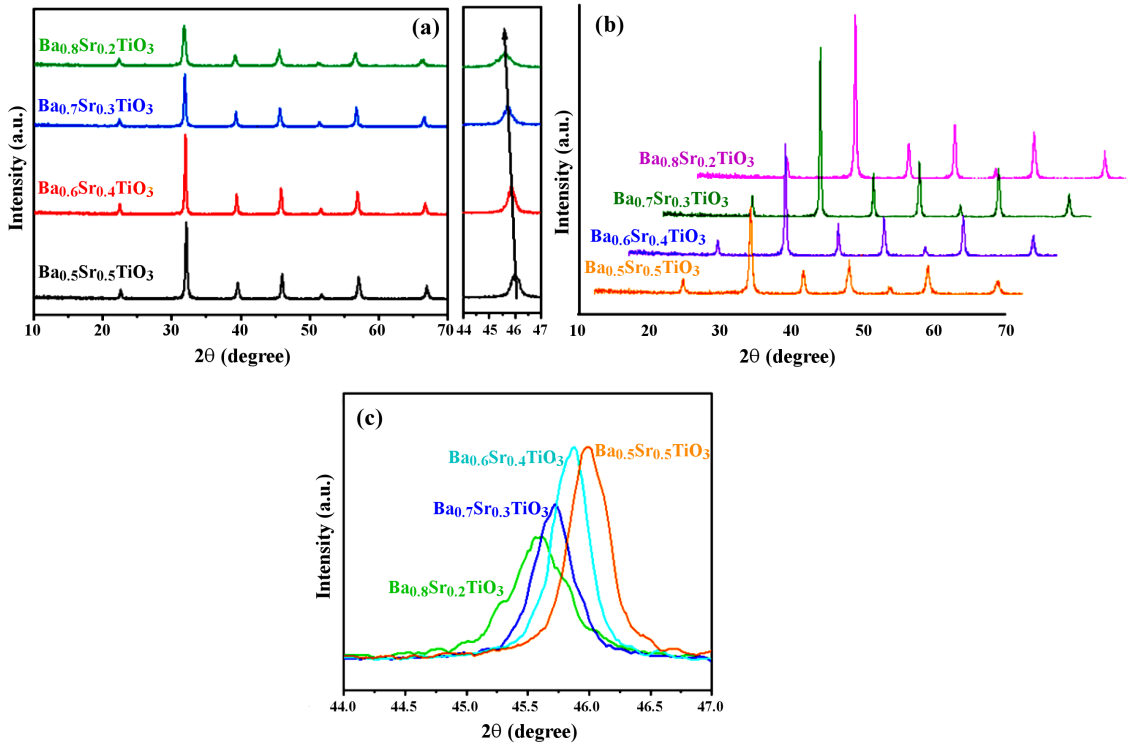

Figure 12. XRD patterns (a) and 3D XRD patterns (b) of samples prepared with different Ba/Sr ratios; magnified region from 44–47° (c)

The diffraction peak also gradually broadens with the increase of Ba content. Due to its limited size, the formed crystal may not be perfect. The difference or deviation of the complete crystallinity leads to the broadening of the diffraction peaks. Two main factors for a peak broadening are microcrystalline size and lattice strain. Table 1 lists the XRD peak analysis results of the samples prepared with different Ba/Sr ratios. The source of lattice strain is mainly attributed to the lattice expansion or lattice contraction in nanocrystals due to the size limitations, because the atomic arrangement changes slightly due to the size limitation compared with their corresponding phase.

The Rietveld refinement of XRD data of the pure phase $Ba_{1-x}Sr_xTiO_3$ powders prepared with different Ba/Sr ratios was also conducted. The Rietveld refinement compares the experimental Bragg intensity with the Bragg intensity calculated by a reasonable structural model and then adjusts the parameters until the best fitness with the experimental diffraction data is obtained [32]. The lattice parameters, unit cell volume and refined parameters calculated from X-ray diffraction data are shown in Table 2. R_p is the full spectrum factor, that is, the variance factor; R_{wp} is the weighted full spectrum factor, representing the weighted figure variance factor; both are descriptions of the fitted results. χ^2 represents the variance value. The R_{wp} values of all $Ba_{1-x}Sr_xTiO_3$ samples are lower than 10%, indicating that there is an excellent agreementt between the experimental results and the theoretical results. The cell parameters and cell

Table 1. Crystallite size calculated by different methods

Sample	Crystallite size [nm]	Williamson-Hall	
		Crystallite size [nm]	Strain
$Ba_{0.8}Sr_{0.2}TiO_3$	17.2	22.5	4.818×10^{-4}
$Ba_{0.7}Sr_{0.3}TiO_3$	24.2	29.2	0.00140×10^{-4}
$Ba_{0.6}Sr_{0.4}TiO_3$	28.0	29.0	0.00177×10^{-4}
$Ba_{0.5}Sr_{0.5}TiO_3$	23.8	33.2	0.00145×10^{-4}

Table 2. Rietveld refinement data obtained for samples with different Ba/Sr ratios

Sample	$BaTiO_3$	$Ba_{0.8}Sr_{0.2}TiO_3$	$Ba_{0.7}Sr_{0.3}TiO_3$	$Ba_{0.6}Sr_{0.4}TiO_3$	$Ba_{0.5}Sr_{0.5}TiO_3$
$a = b = c$ [Å]	4.0073	3.9926	3.9869	3.9704	3.9619
$\alpha = \beta = \gamma$	90.00	90.00	90.00	90.00	90.00
Volume [Å^3]	64.351	63.788	63.488	62.590	62.188
R_{wp}		8.35	8.61	8.36	8.70
R_p		5.57	6.05	5.81	6.13
χ^2		1.712	1.895	1.778	2.080
Ba–O [Å]		2.8253	2.8215	2.8074	2.8015
Ti–O [Å]		1.9978	1.9951	1.9852	1.9809

volumes of all samples are smaller than those of $BaTiO_3$ (JCPDS 05-0626). The lattice constants and cell volumes decrease gradually with the increase of strontium content because the ion radius of Sr^{2+} is smaller than that of Ba^{2+}. The calculated bond lengths are also given in the table. With the increase of Sr content, the bond length of Ba–O/Ti–O decreases gradually. It can also be verified according to the size of the ion radius.

IV. Conclusions

$Ba_{1-x}Sr_xTiO_3$ nanopowders were synthesized via nonhydrolytic sol-gel method and the effects of different processing parameters on structure were systematically investigated. Among three different dispersants, the smallest particles with uniform distribution were obtained with Tween 60. The dispersibility and uniformity were optimal when 1.0 wt.% of Tween 60 was used as the dispersant. Moreover, the results of mass spectroscopy and laser particle size distribution analysis show that the optimized calcination temperature was 900 °C at which crystalline phase was formed and all organic groups were removed. The pure phase $Ba_{0.5}Sr_{0.5}TiO_3$ and $Ba_{0.6}Sr_{0.4}TiO_3$ powders can be prepared when (Ba+Sr)/Ti = 1/1.2, while higher ratio is necessary for the samples with lower Sr content. Thus, the pure phase $Ba_{0.7}Sr_{0.3}TiO_3$ and $Ba_{0.8}Sr_{0.2}TiO_3$ can be prepared when (Ba+Sr)/Ti ratios are 1/1.3 and 1/1.4, respectively. All pure phase powders have cubic perovskite structure due to small particles and the size effect. The lattice constants and cell volumes of cubic phase decrease gradually with the increase of Sr content. This study confirms that the ultra-fine BST nanopowders with narrow size distribution can be prepared by optimizing important process parameters.

Acknowledgements: This work was supported by the National Natural Science Foundation of China [grant numbers 52072162, 51962014, 52262003, 52362041]; Jiangxi Provincial Natural Science Foundation [grant numbers 20202ACBL214006, 20202ACBL214008, 2020ZDI03004, 20202BABL214013, 20232ACB204012]; the Projects of Jiangxi Provincial Department of Science and Technology (20202BABL214013); the Science Foundation of Jiangxi Provincial Department of Education (GJJ211308).

References

1. M.E.A. Araghi, N. Shaban, M. Bahar, "Synthesis and characterization of nanocrystalline barium strontium titanate powder by a modified sol-gel processing", *Mater. Sci. Poland*, **34** [1] (2016) 63–68.
2. V. Somani, S.J. Kalita, "Synthesis and characterization of nanocrystalline barium strontium titanate powder via sol-gel processing", *J. Electroceram.*, **18** (2007) 57–65.
3. Z.Y. Shen, Y. Wang, Y.X. Tang, Y.Y. Yu, W.Q. Luo, X.C. Wang, Y.M. Li, Z.M. Wang, F.S. Song, "Glass modified barium strontium titanate ceramics for energy storage capacitor at elevated temperatures", *J. Materiomics*, **5** [4] (2019) 641–648.
4. E.G. Erker, A.S. Nagra, L. Yu, P. Periaswamy, T.R. Taylor, J. Speck, R.A. York, "Monolithic Ka-band phase shifter using voltage tunable $BaSrTiO_3$ parallel plate capacitors", *IEEE Microw Guided W*, **10** [1] (2000) 10–12.
5. R.S. Yaduvanshi, "Design and analysis of superstrate embedded dielectric resonator antenna", *Int. J. Commun. Syst.*, **3** [1] (2014) 31–37.
6. L. Yu, A.S. Nagra, E.G. Erker, P. Periaswamy, T.R. Taylor, J. Speck, R.A. York, "$BaSrTiO_3$ interdigitated capacitors for distributed phase shifter applications", *IEEE Microw Guided W*, **10** [11] (2000) 448–450.
7. G. Panomsuwan, H. Manuspiya, "Morphological and structural properties of barium strontium titanate nanopowders synthesized via a sol-gel method", *Ferro-*

electrics, **554** [1] (2020) 30–37.
8. J.M. Siqueiros, J. Portelles, S. Garcıá, M. Xiao, S. Aguilera, "Study by hysteresis measurements of the influence of grain size on the dielectric properties of ceramics of the $Sr_{0.4}Ba_{0.6}TiO_3$ type prepared under different sintering conditions", *Solid State Commun*., **112** [4] (1999) 189–194.
9. L. Zhang, L. Zhong, C.L. Wang, P.L. Zhang, Y.G. Wang, "Dielectric Properties of Ba0.7Sr0.3TiO3 Ceramics with Different Grain Size", *Phys Status Solidi A*, **168** (1998) 543–548.
10. S.W. Lu, B.I. Lee, Z.L. Wang, W.D. Samuels, "Hydrothermal synthesis and structural characterization of $BaTiO_3$ nanocrystals", *J. Cryst. Growth*, **219** [3] (2000) 269–276.
11. S. Karthikeyan, P. Thirunavukkarasu, S. Surendhiran, A. Balamurugan, Y.A.S. Khadar, K. Shanmugasundaram, "Facile synthesis of barium strontium titanate: Effects of processing parameters on optical and electrical properties", *Mater. Today Proceed*., **47 [**4] (2021) 964–969.
12. L. Wu, Y.C. Chen, L.J. Chen, Y.P. Chou, Y.T. Tsai, "Preparation and microwave characterization of $Ba_xSr_{1-x}TiO_3$ ceramics", *Jpn. J. Appl. Phys*., **38** (1999) 5612.
13. X. Wei, G. Xu, Z.H. Ren, Y.G. Wang, G. Shen, G. Han, "Composition and shape control of single-crystalline $Ba_{1-x}Sr_xTiO_3$ (x = 0–1) nanocrystals via a solvothermal route", *J. Cryst. Growth*, **310** [18] (2008) 4132–4137.
14. R.K. Roeder, E.B. Slamovich, "Stoichiometry control and phase selection in hydrothermally derived $Ba_xSr_{1-x}TiO_3$ powders", *J. Am. Ceram. Soc*., **82** [7] (1999) 1665–1675.
15. X.F. Zhang, Q. Xu, Y.H. Huang, H.X. Liu, D.P. Huang, F. Zhang, "Low-temperature synthesis of superfine barium strontium titanate powder by the citrate method", *Ceram. Int*., **36** [4] (2010) 1405–1409.
16. B. Wodecka-Duś, A. Lisińska-Czekaj, T. Orkisz, M. Adamczyk, K. Osińska, L. Kozielski, D. Czekaj, "The sol-gel synthesis of barium strontium titanate ceramics", *Mater. Sci. Poland*, **25** [3] (2007) 791–799.
17. Y. Wang, Z.Y. Shen, Y.M. Li, Z.M. Wang, W.Q. Luo, Y. Hong, "Optimization of energy storage density and efficiency in $Ba_xSr_{1-x}TiO_3$ ($x \leq 0.4$) paraelectric ceramics", *Ceram. Int*., **41** [6] (2015) 8252–8256.
18. L. Yin, F. Jiang, G. Feng, C. Wu, J.G. Tan, Q. Wu, R.C. Zhang, W.H. Jiang, "Effects of process parameters on nonhydrolytic sol-gel synthesis of $Ba_{0.6}Sr_{0.4}TiO_3$ powders", *Ceram. Int*., **48** [19] (2022) 28274–28281.
19. Y. Zhang, M.Q. Ye, A. Han, C. Ding, J.L. Yang, K. Zhang, "Preparation and characterization of encapsulated $CoAl_2O_4$ pigment and charge control agent for ceramic toner via suspension polymerization", *Ceram. Int*., **44** [16] (2018) 20322–20329.
20. C.G. Yáñez, H.B. Ramírez, F. Martínez, "Colloidal processing of $BaTiO_3$ using ammonium polyacrylate as dispersant", *Ceram. Int*., **26** [6] (2000) 609–616.
21. C.H. Yeh, M.H. Hon, "Dispersion and stabilization of aqueous TiC suspension", *Ceram. Int*., **21** [2] (1995) 65–68.
22. S. Satyendra, S.B. Krupanidhi, "Synthesis and structural characterization of $Ba_{0.6}Sr_{0.4}TiO_3$ nanotubes", *Phys. Lett. A*, **367** [4] (2007) 356–359.
23. M.M. Vijatović Petrović, J.D. Bobic, T. Ramoska, J. Banys, B.D. Stojanović, "Electrical properties of lanthanum doped barium titanate ceramics", *Mater. Charact*., **62** [10] (2011) 1000–1006.
24. Q.Q. Zhao, G. Feng, F. Jiang, S.F. Lan, J.H. Chen, F.F. Zhong, Z.Z. Huang, H. PAN, J.M. Liu, Q. Hu, W.H. Jiang, "Nonhydrolytic sol-gel in-situ synthesis of novel recoverable amorphous Fe_2TiO_5/C hollow spheres as visible-light driven photocatalysts", *Mater. Des*., **194** (2020) 108928.
25. L. Yin, F. Jiang, G. Feng, C. Wu, J.G. Tan, Q. Wu, Q. Zhang, Q. Hu, J.M. Liu, W.H. Jiang, "Effects of raw materials on nonhydrolytic sol-gel synthesis of $Ba_{0.6}Sr_{0.4}TiO_3$", *Ceram. Int*., **48** [18] (2022) 25681–25688.
26. R. Jacob, J. Isac, "X-ray diffraction line profile analysis of $Ba_{0.6}Sr_{0.4}Fe_xTi_{1-x}O_{3-\delta}$ (x = 0.4)", *Int. J. Chem. Stud*., **2** [5] (2015) 12–21.
27. Q.W. Zhang, J.W. Zhai, B. Shen, H.J. Zhang, X. Yao, "Grain size effects on dielectric properties of barium strontium titanate composite ceramics", *Mater. Res. Bull*., **48** [3] (2013) 973–977.
28. Q.A. Zhu, Y. Wu, X.F. Sun, X. Tan, K. Zhan, J.H. Cai, "Synthesis and characterization of barium strontium titanate nanocrystalline powders prepared by direct reactive precipitation method from solution". *Adv. Mat. Res*., **634** [1] (2013) 2301–2306.
29. M. Enhessari, A. Parviz, K. Ozaee, H. Habibi Abyaneh, "Synthesis and characterization of barium strontium Titanate (BST) micro/nanostructures prepared by improved methods", *Int. J. Nano Dim*., **2** [1] (2011) 85–103.
30. N.J. Ridha, W.M.M. Yunus, A.H. Shaari, Z.A. Talib, F.K.M. Al-Asfoor, W.C. Primus, "Effect of Sr substitution on structure and thermal diffusivity of $Ba_{1-x}Sr_xTiO_3$ ceramic", *Am. J. Appl. Sci*., **2** [4] (2009) 661–664.
31. C. Baek, J.E. Wang, D.S. Kim, D.K. Kim, "Hydrothermal synthesis and dielectric properties of $Ba_{1-x}Sr_xTiO_3$ nanoparticles with enhanced uniformity", *J. Nanosci. Nanotechno*., **16** [11] (2016) 11652–11657.
32. V. Petkov, M. Gateshki, M. Niederberger, Y. Ren, "Atomic-scale structure of nanocrystalline $Ba_xSr_{1-x}TiO_3$ (x = 1, 0.5, 0) by X-ray diffraction and the atomic pair distribution function technique", *Chem. Mater*., **18** [3] (2006) 814–821.